

Light-Powered Micromotor: Design, Fabrication, and Mathematical Modeling

Li-Hsin Han, Shaomin Wu, J. Christopher Condit, Nate J. Kemp, Thomas E. Milner, Marc D. Feldman, and Shaochen Chen

Abstract—This paper reports on the experimental and theoretical studies of a light-driven micromotor, which is a “light mill” that rotates by absorbing photon energy. This light mill has four curved blades to form an axially asymmetric geometry. Upon lateral irradiation, the shape of the light mill induces an asymmetric photon heating to the surrounding gas molecules, leading to a gas convection that forces the light mill to rotate. The light mill was applied to actuate a scanning mirror for a laser beam. Using a Direct Simulation Monte Carlo (DSMC) model, we investigated the working principle behind the operation of the light mill. The DSMC simulation yielded results consistent to our experimental data. The simulation results were used to explain the heat-induced light-mill rotation, in which the mean free path of the surrounding gas takes an important role. [2010-0149]

Index Terms—Crookes, DSMC, light mill, microactuator, micromotor, Monte Carlo, nanoparticles.

I. INTRODUCTION

A. Light as a Power Source for Microactuators

THE STUDIES of light-powered micromachines have gained considerable attention during the recent years [1], [2]. Light-powered micromachines are driven by the absorption of electromagnetic wave, a conversion of photon energy into kinetic power, and the subsequent discharge of heat. Because the principle of these light-powered micromachines includes no mass flow or electric current, a considerable space otherwise needed for peripheral elements, such as microchannels, micropumps, or wirings, is saved. The simplicity of light-powered machine promotes standing-off microsystems, actuator miniaturization, and wireless power delivery; these features

Manuscript received May 26, 2010; revised October 11, 2010; accepted November 14, 2010. Date of publication February 14, 2011; date of current version April 1, 2011. The work of S. Chen was supported by grants from the Office of Naval Research (N00014-07-1-0609) and the National Science Foundation (CMMI 0555275). Subject Editor L. Lin.

L.-H. Han is with the Department of Orthopaedic Surgery, Stanford University, Stanford, CA 94305 USA (e-mail: leohan17@gmail.com).

S. Wu is with Materials Science and Engineering, The University of Texas at Austin, Austin, TX 78712 USA (e-mail: wushaomin@yahoo.com).

J. C. Condit and T. E. Milner are with the Department of Biomedical Engineering, The University of Texas at Austin, Austin, TX 78712 USA (e-mail: condit.chris@gmail.com; terra.laser@gmail.com).

N. J. Kemp is with Volcano Corporation, Billerica, MA 01821 USA (e-mail: natekemp@gmail.com).

M. D. Feldman is with the Department of Medicine, The University of Texas Health Science Center, San Antonio, TX 78229 USA, and also with the South Texas Veterans Health Care System, San Antonio, TX 78229 USA.

S. Chen is with the Department of Nanoengineering, University of California, San Diego, La Jolla, CA 92093 USA (e-mail: shc064@ucsd.edu).

Color versions of one or more of the figures in this paper are available online at <http://ieeexplore.ieee.org>.

Digital Object Identifier 10.1109/JMEMS.2011.2105249

for microactuators are important to many advanced applications for biomedical, mechanical, and aerospace engineering [3]–[5].

B. Research Motivation

Our study for light-powered micromotors was motivated by the development of a cardiovascular-imaging system to investigate the cross-sectional distribution of human coronary arterial tissues [6]. This system includes an endoscope catheter, which is inserted from a femoral artery to reach the lumen of coronary arteries by a diagnostic tip. Along an optical fiber in the catheter, a near-infrared (NIR) laser beam is delivered to the diagnostic tip and is focused to generate scattering spots in the tissues at different levels of the arterial wall [7]. The scattered light is recollected by the optical fiber, guided to the outside of the human body, and delivered to a photo analyzer. The analyzer measures the phase and the intensity of light from each scattering, calculates the optical properties of the tissues at each location, and produces data to image the spatial distribution of different matters, including arterial tissues, lipid pools, and athermanous plaques, in the arterial wall. To obtain a cross-sectional image, a rotating mechanism, such as a rotating micromirror, is needed to scan the NIR laser over the surrounding arterial wall. We calculated that the speed of rotation should be at least several hundred rounds per minute (rpm) for a reasonable operation time in a clinical practice, which requires taking continuous cross-sectional images along a length of an artery. An electric micromotor could generate the required rotation; however, using electricity inside coronary arteries is undesirable due to the risk of disrupting the heart by leaked voltage or electrostatic discharge. A micromotor using an alternative power source, such as light, is preferred for this type of applications.

C. Crookes' Light Mill

The Crookes radiometer [Fig. 1(a)], also known as light mill, was created in the 19th century and became the earliest light-powered actuator [8], [9]. The light mill has several asymmetrically colored blades; each blade has one side that is dark and the other side that is bright. Upon irradiation in reduced air pressure (1–0.01 torr), the blades turn with the dark sides retreating from the source of light. The working principle of the light mill is based on the convection of gas molecules induced by an asymmetric photon heating; the dark sides of the blades absorb more photon energy from light and deliver more heat to the surrounding gas molecules. This asymmetric photon heating

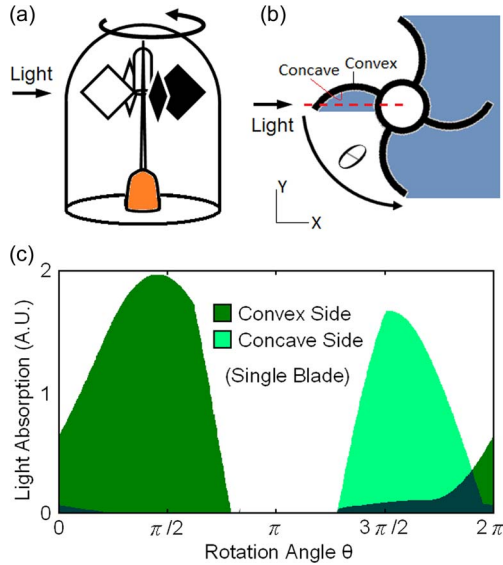


Fig. 1. (a) Illustration of the Crookes Mill. (b) The design for a light mill with a homogeneous-surface property. (c) Calculated light absorption by the different sides of a single blade (as a function of light-mill rotation angle from 0 to 2π); the light mill at (b) shows the initial angle, at which $\theta = 0$.

generates a gradient of gas temperature across the blade, causing gas convection and inducing blade rotation. The mechanism of the light mill is promising to the development of light-powered microactuators. However, in spite of the advanced technology of semiconductor-based microfabrication and nanofabrication [3]–[5], the original design of the Crookes' Mill is difficult to miniaturize; it requires efforts to pattern materials of distinct optical properties at different spatial locations within a thin three-dimensional (3-D) space.

D. Reinventing the Light Mill: An Alternative Design

While the Crookes' Mill remains an educational tool for more than a hundred years after being invented, few have questioned the necessity of the heterogeneous optical property at the blades to its light-driven rotation. In this paper, we demonstrate that a uniformly dark "turbine-shaped" miniature light mill can perform high-speed spinning upon irradiation. This light mill rotates based on a geometry-induced asymmetric photon heating of the surrounding gas [Fig. 1(b)]. This simplified design promotes the miniaturization of light mill and the application of light mill to the development of light-powered micromachines.

II. DESIGN AND FABRICATION OF THE LIGHT-POWERED MICROMOTOR

A. Light Mill Powered by Geometry-Assisted Asymmetric Photon Heating

The light mill we created, which was previously reported [10], has four blades; each blade is curved to form convex and concave sides. This geometry causes different rates of photon heating on the two sides of the blade upon lateral irradiation [Fig. 1(b)]. We simulated the amount of irradiation at the two surfaces of a single blade by integrating the inner product between the surface normal and the vector of incident light (along the X -axis). At any rotation angle, if the light vector

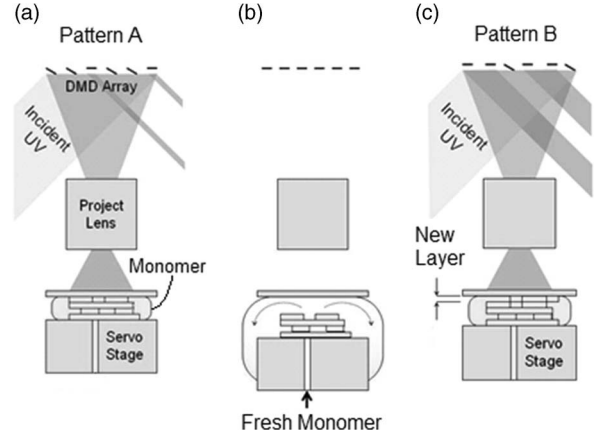


Fig. 2. Schematic fabrication sequence showing the development of a 3-D microstructure using DMD-PP.

passes any surface before reaching the calculated surface, the light is considered "blocked" and the product is set zero. The calculation result shows that the absorption by the convex side is higher than twice the absorption by the concave side [Fig. 1(c)]. Consequently, the convex side of the blade transfers more heat from light to the surrounding gas, leading to a temperature difference across the blade for driving the gas molecules, which forces the light mill to rotate.

B. DMD-PP Microfabrication System to Create the Light Mill

We fabricated the light mill using a Digital Micromirror Device Projection Printing (DMD-PP) system [11], [12] (Fig. 2). The DMD-PP system fabricates 3-D objects by creating a sequence of cross-sectional slices from a photocurable monomer. The DMD-PP fabrication starts by developing a digital 3-D-model, splitting the model into continuous cross-sectional slice images, and sending the data of the slice images to a dynamic mask of the DMD-PP system. In the dynamic mask are hundreds of thousands of micromirrors arranged in a rectangular array; to form a mask image, the micromirrors are rotated electrically to an "ON" or "OFF" state according to the pixels of a slice image. The micromirrors in the ON state reflect an ultraviolet (UV) illumination toward a lens, which projects the reflected light as a bright image to cure the monomer. A 3-D structure is developed by continuously creating cross-sectional layers from the monomer according to a sequence of slice images [Fig. 2(a)–(c)]. Limited only by the quality of the projection lenses, the smallest feature the DMD-PP system can possibly fabricate is sized by the diffraction limit of the curing light, which is on the order of $1 \mu\text{m}$.

Our DMD-PP system [Fig. 3(a)] includes a servo stage (CMA-25-CCCL & ESP300, Newport), a syringe pump, a fluorinated glass window, a DMD chip and control board (Discovery 1100, Texas Instruments), a UV lamp (200 W, S2000, EXFO), and a UV-grade projection lens (NT57-541 Megapixel, Edmond Optics). The syringe pump injects a photocurable monomer to the servo stage. The DMD chip has an array (1024 by 768) of micromirrors to form the dynamic-mask. The micromirrors are illuminated by UV light from the lamp using an 8-mm light guide. Upon illumination, the UV images

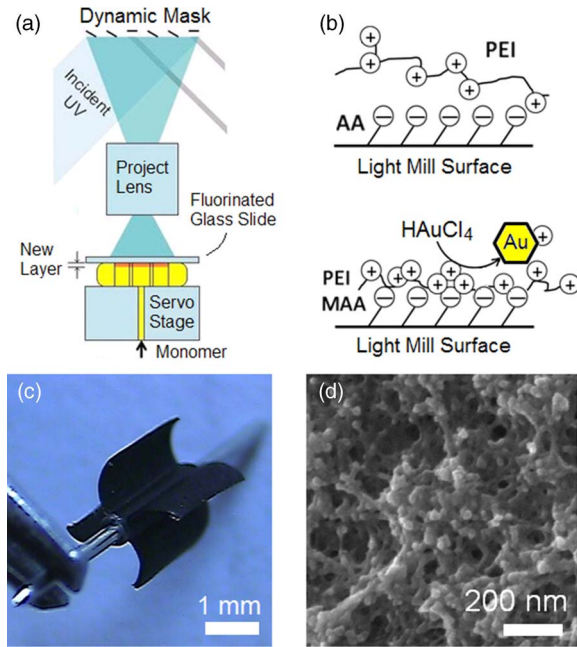


Fig. 3. Fabrication of the light mill. (a) Setup of our DMD-PP system. (b) Postfabrication process to form closely packed gold nanoparticles on the surface of the light mill. (c) A fabricated light mill held by a pair of tweezers. (d) A SEM image showing the closely packed gold nanoparticles in the submicrometer pores on the light-mill surface.

of the reflective patterns are projected onto the photocurable monomer by the projection lens. The monomers, loaded above the servo stage, are selectively cured by the UV images and form microstructure layers.

The glass window is fixed right above the microstructure and is also at the focal point of the projection lens. Before UV-exposure, the monomers are pumped to fill the space between the window and the microstructure, which controls the thickness of the microstructure layers. Upon UV illumination, the monomer layers below the window are cured selectively, resembling the pattern of the micromirror array. The window is coated with (tridecafluoro-1,1,2,2-tetrahydrooctyl) trichlorosilane, a fluorinated agent, to release the microstructure from the window surface after UV curing. The coating process for the glass window is reported elsewhere [13]. The servo stage, the syringe pumps, the DMD chipset, and the UV lamp are connected to a personal computer (PC), with the DMD-PP system being controlled by the PC through programming.

C. Material Preparation and Light-Mill Fabrication

The photocurable monomer to develop the light mill was prepared by adding 1% photoinitiator Irgacure 651 (Ciba Chemistry), 0.5% UV absorber TINUVIN 234 (Ciba Chemistry), and 0.02% radical quencher 2,2,6,6-tetramethylpiperidine 1-oxyl in a mixture of 60 wt% polyethylene glycol (MW = 700), 20 wt% acrylic acid, and 20 wt% zinc acrylate (Sigma-Aldrich).

The fabrication of the light mill follows the aforementioned procedures. The DMD chip was patterned according to the designed cross section of the light mill [see Fig. 1(b)]. After the first layer of the light mill was developed, the stage was repositioned downward until the top of the structure was situated

one-layer thick ($50 \mu\text{m}$ below the glass-slide). Fresh monomer was then pumped into the gap to replace the used monomer. The previous steps were repeated until a light mill of 3-mm height was built. The DMD-PP fabrication process for the light mill took about 30 min. The final dimensions of the light mill are as follows: axial length: 3 mm; center-hole diameter: $400 \mu\text{m}$; arc length of blade: 1 mm; and blade tangential angle: 90° .

D. Postfabrication: Closely Packed Gold Nanoparticles as Photoabsorption Coating

After DMD-PP microfabrication, the as-formed light mill was rinsed in diluted HCl (pH = 2) for 2 h to remove zinc ions from the material matrix, leaving behind nanoscaled porosity. After washing by water, the light mill was rinsed for 1 h in 1% polyethyleneimine (PEI, MW = 800, from Sigma-Aldrich). The positively charged PEI molecules readily attached to the carboxylic groups (from acrylic acid and the hydrolyzed zinc acrylate) at the surfaces in the nanopores. The PEI-treated light mill was subsequently rinsed in 0.1% HAuCl_4 water solution, at 85°C , for 90 s. The formation of nanoparticles causes drastic color change [from bright to dark, Fig. 3(c)]. This reaction produces metallic gold, resulting in closely packed gold nanoparticles (diameter $< 50 \text{ nm}$) in the micropores [Fig. 3(d)]. After the coating, the light mill became uniformly dark and strongly light absorbing due to electrodynamic interactions among the dense gold nanoparticles [14]. Having a large internal surface for heat transfer, the micropores with gold nanoparticles become an efficient light-powered heater for the surrounding gas molecules.

III. TURNING THE LIGHT MILL BY LIGHT

A. Light-Driven Light-Mill Rotation

Fig. 4 shows the setup for our experiment. We inserted a pin shaft ($400 \mu\text{m}$ in diameter) through a center hole of the light mill. The light mill with the pin shaft was mounted between a pair of V-jewel bearings (Small Parts Corporation), which held point contacts with the pin heads of the shaft to minimize friction. A Teflon holder was used to fix the light-mill assembly in a glass vacuum chamber. A vacuum pump (capacity: 30 mtorr) was connected to create an environment of rarified gas in the chamber, and the air pressure in the chamber was made adjustable by using a needle valve. A white-light source was installed to illuminate the blade surfaces of the light mill. The movements of the blades were detected by using an optical position sensor (DLD sensor, MICROTRAK), which has a frequency bandwidth of 20 kHz and movement sensitivity below $1 \mu\text{m}$. The signal from the position sensor was sent to an oscilloscope (500-MHz bandwidth and a one-billion-sample-per second sampling rate) to record the rotation of the blades. The rotation speed of the light mill was determined based on the recorded waveform from the oscilloscope

$$\omega(\text{rpm}) = \frac{N_{\text{cycle}}}{t} \times 60 \div N_{\text{blade}} \quad (1)$$

where N_{cycle} is the number of cycles of the signal, t is the time span of the signal in seconds, and N_{blade} , which is equal to four, stands for the number of the light-mill blades.

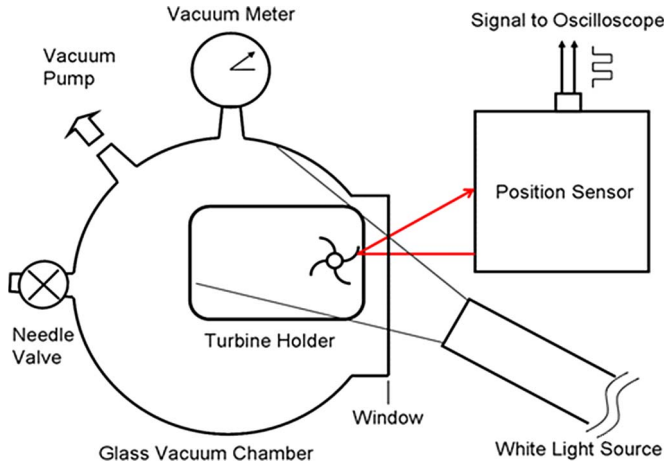


Fig. 4. Experiment setup to investigate the operation of the light mill.

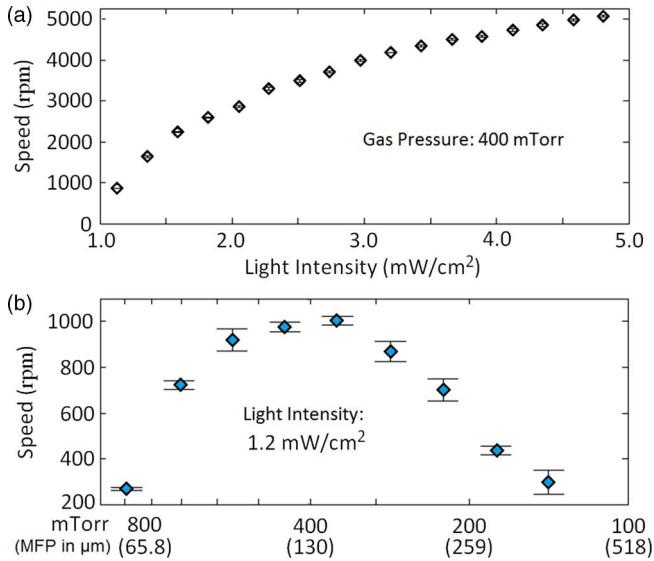


Fig. 5. Experiment results: (a) Light-mill speed versus irradiation intensity at a constant pressure (400 mtorr) and (b) light-mill speed versus air pressure at constant irradiation (1.2 mW/cm^2). Each error bar indicates standard deviation of five measurements.

The light mill spins rapidly with the convex surfaces retreating from the source of light. Measurement by the DLD sensor shows that the rotation speed varied from several hundreds to thousands of rpm, depending on the light intensity and also on the degree of vacuum [Fig. 5(a) and (b)]. For white-light illumination, the rotation speed was maximized at about 400 mtorr, corresponding to a mean free path (MFP) of air of $130 \mu\text{m}$ [15]

$$MFP_{\text{Air}}(\mu\text{m}) \cong \frac{5 \times 10^4}{\text{pressure}(\text{morr})}, \quad 20^\circ\text{C}. \quad (2)$$

Because the light mill ceases to spin at lower pressure, we conclude that the observed rotation does not stem from the Yarkovsky effect, namely, the recoil momentum from thermally irradiated photons [16]. The experiment result is, however, consistent with the calculation by Einstein [8], who concluded that the net force exerted on a light mill is from heat-induced gas

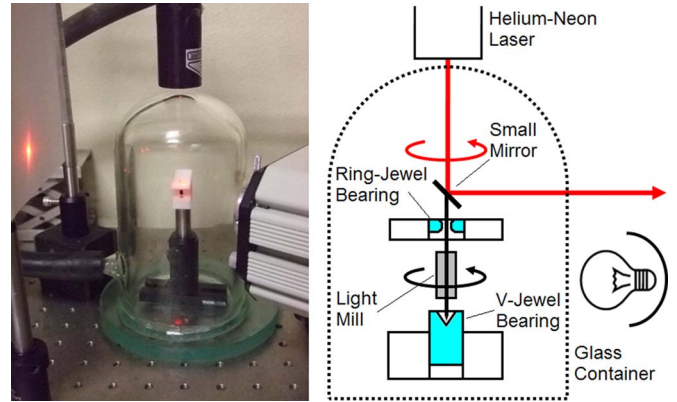


Fig. 6. Application of the light mill: light-powered scanning mirror for a helium-neon laser beam (online video available at JMEMS Website).

momentum and is maximized when the MFP of the surrounding gas becomes comparable with the thickness of the blades of the light mill, which is $75 \mu\text{m}$ in this case.

B. Light-Driven Rotation of Small Mirror for Laser Scanning

Fig. 6 shows the setup for a light-powered rotating mirror driven by the light mill. We fabricated a small mirror (1.5 mm by 1.5 mm) by coating platinum (50 nm thick) on a glass slide using plasma sputtering. The small mirror was glued to one end of the pin shaft of light mill; the angle between the surface of the mirror and the pin shaft was about 45° . On a Teflon holder, the shaft was mounted between a V-jewel bearing and a ring-jewel bearing (Swiss Jewel Company), which left an opened end to the pin shaft to install the mirror. A helium–neon laser (640 nm) beam propagating parallel to the shaft was applied to the small mirror and reflected laterally.

When a white-light irradiation was applied to the assembly, the small mirror spins and performs laser scanning. This experiment demonstrates the potential applications of our light-mill system; for example, this scanning mirror can be applied to develop the aforementioned cardiovascular imaging system. A video about this experiment is available online [17].

IV. INVESTIGATING THE GAS DYNAMICS BEHIND THE LIGHT-MILL ROTATION

A. DSMC Method

A gas-dynamics model could be developed based on either a continuous Navier–Stokes approach [18] or a discrete molecular-dynamics calculation [19]. Although a Navier–Stokes approach is much more computationally economical compared with the molecular-dynamics calculation, one should first evaluate the validity of both methods based on the physics of the simulated system.

The validity of using the Navier–Stokes equation depends on a characteristic dimension L of the gas flow and also on the MFP λ of the gas molecules [20]. L is defined as the length of a physically important macroscale gradient of dynamics variables, such as velocity or temperature. λ is the average distance that a molecule travels between two sequential collisions, which

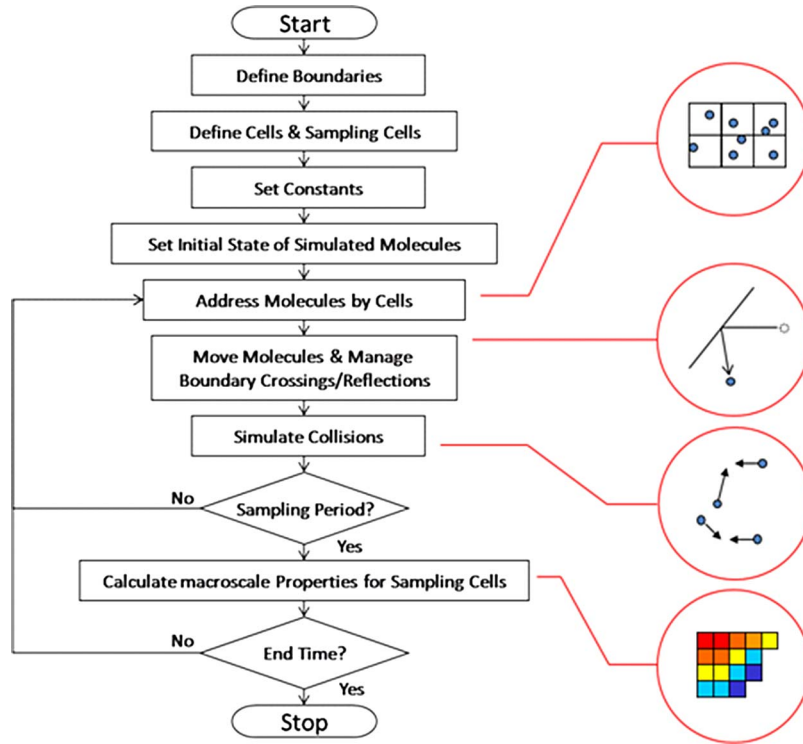


Fig. 7. Flowchart for a typical DSMC program.

change the velocity of the molecule. A continuum approach assumes that the fluctuations of the dynamics variables among individual molecules can be averaged to build a smooth gradient over the dimension L . The validity of this assumption is checked by a rule of thumb given by [21]

$$\lambda/L < 0.1. \quad (3)$$

When $\lambda/L > 0.1$, the fluctuations in the gradient are considered important, and it becomes necessary to consider the microscopic gas dynamics within the gradient space. Another guideline to check the validity of the continuum approach is a ratio between L and the average molecule spacing δ

$$L/\delta > 100. \quad (4)$$

Outside this limit, the Navier–Stokes approach is considered invalid, and a complete microscopic approach should be used instead.

For our light-mill system, we conclude that the sharpest gradient is created at the edges of each blade, where the distinct surface temperatures meet. This dimension is physically important, for this temperature gradient directly leads to the gas convection that drives the light mill. Therefore, the blade thickness ($75 \mu\text{m}$) is used for our characteristic dimension L . The next step is to calculate λ and δ . Our light mill spins at a range of air pressure from 10 to 1000 mtorr. In this range and at room temperature (25°C), λ and δ are [21]

$$5.187 \times 10^{-5} \text{ m} < \lambda_{\text{LightMill}} < 5.187 \times 10^{-3} \text{ m} \quad (5)$$

$$3.137 \times 10^{-8} \text{ m} < \delta_{\text{LightMill}} < 1.456 \times 10^{-7} \text{ m}. \quad (6)$$

Using the guideline equations (3) and (4) to check the validity of the Navier–Stokes approach, we obtain

$$0.6917 < \lambda_{\text{LightMill}}/L < 6.917 \quad (7)$$

$$515.1 < L/\delta_{\text{LightMill}} < 2391. \quad (8)$$

The result shows that, in this pressure range, the first guideline equation (3) is failed by more than one order, and the second (4) is met only marginally. The Navier–Stokes approach is thus not appropriate for our light-mill system; a molecular-dynamics approach is required.

Developed by Bird, the Direct Simulation Monte Carlo (DSMC) method is a molecular-dynamics model based on the statistical mechanics of gas molecules [19]. In DSMC, realistic gas molecules in a physical space are simulated by a smaller number of representative molecules. The positions and velocities of the molecule in the physical space are calculated at a sequence of time steps. At each time step, representative collisions among the simulated molecules and between the molecules and the system boundaries are simulated. The location of collision events, the selection of collision pairs, and the postcollision velocities of the colliding molecules are calculated based on the law of energy conservation, momentum conservation, and on the theoretical distribution of probable values for the dynamics system. The physics properties, such as pressure and temperature, are sampled by multiple subspaces (or cells) in the whole simulation domain. Fig. 7 shows a flowchart of a typical DSMC simulation. Compared with the simulations of complete molecular dynamics, the DSMC method is computationally economical and suitable for a system of much

larger scale. We report the details of our DSMC modeling as follows.

1) *Newtonian and Statistical Dynamics About Collisions Between Hard-Spheres*: For simplicity, the collisions among gas molecules in the simulation space were simulated as the collisions among identical hard spheres, which are elastic and frictionless [20]; delay in the velocity change of the colliding particles is absent. By using this approximation, the dynamics of collision involves exclusively Newtonian mechanics, which demands only the conservation of kinetic energy and particle momentum. The hard-sphere model is most accurate for the problems of single-atom gas, nonpolar molecules, and chemically inert species. One of the good examples is the argon gas. For fluids of other kinds, the approximation by using hard-sphere model also becomes recommendable when the simulated molecule is a rarified gas. A rule of thumb to judge whether the hard-sphere approximation is suitable for the problem is by comparing the MFP (λ) of a group of simulated molecules with their effective molecular diameters (D , $\sim 3 \times 10^{-10}$ m) [21]

$$\lambda \gg D. \quad (9)$$

The light mill is operated under rarefied-gas environment in which $\lambda \gg D$; thus, the criteria for using hard-sphere model is satisfied.

2) *Newtonian Dynamics of a Pair of Colliding Hard Spheres*: Given that \vec{V}_1 and \vec{V}_2 are the initial velocities of two colliding identical hard-spheres, the velocities after collision \vec{V}'_1 and \vec{V}'_2 are related to \vec{V}_1 and \vec{V}_2 using energy and momentum conservation

$$|\vec{V}_1|^2 + |\vec{V}_2|^2 = |\vec{V}'_1|^2 + |\vec{V}'_2|^2 \quad (10)$$

$$\vec{V}_1 + \vec{V}_2 = \vec{V}'_1 + \vec{V}'_2. \quad (11)$$

By introducing the velocity of the mass center of the two spheres \vec{V}_{cm} and the relative velocity between the spheres \vec{V}_r , \vec{V}_1 and \vec{V}_2 becomes

$$\vec{V}_1 = \vec{V}_{cm} + \vec{V}_r \quad (12)$$

$$\vec{V}_2 = \vec{V}_{cm} - \vec{V}_r \quad (13)$$

where $\vec{V}_{cm} = (\vec{V}_1 + \vec{V}_2)/2$ and $\vec{V}_r = (\vec{V}_1 - \vec{V}_2)/2$.

Following the law of momentum conservation, \vec{V}_{cm} remains unchanged after collision, so \vec{V}'_1 and \vec{V}'_2 become

$$\vec{V}'_1 = \vec{V}_{cm} + \rightarrow V'_r \quad (14)$$

$$\vec{V}'_2 = \vec{V}_{cm} - \rightarrow V'_r. \quad (15)$$

The law of energy conservation requires that $|\vec{V}'_r| = |\vec{V}_r|$. The new velocities for the colliding hard spheres are normal to the collision plane, at which the pair have point contact at the moment of colliding. Therefore, the unknown variables

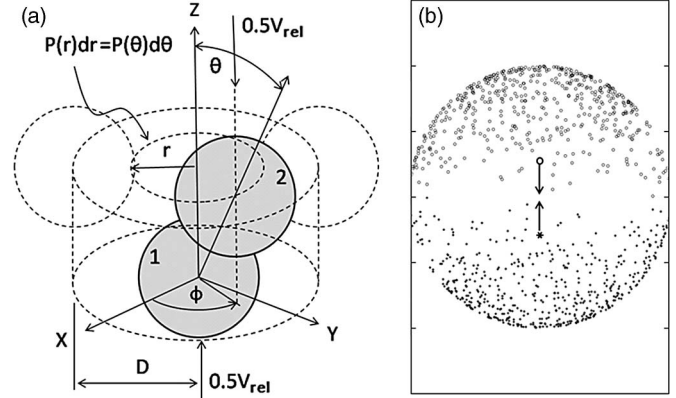


Fig. 8. (a) The rebound movements of colliding particles depend on their collision angles (θ, ϕ) and relative speed V_{rel} . (b) Simulated rebound movements of a pair of colliding particles with random collision angles (θ, ϕ) .

are reduced to the collision angles (θ, ϕ) , at which the spheres contact each other at the moment of collision [Fig. 8(a)].

One needs to know the relative position of the colliding spheres to calculate the exact values of (θ, ϕ) for each colliding pair. In a simulation domain that contains many particles, however, the colliding angles (θ, ϕ) for each pair of colliding particles are randomly generated based on statistical distribution to gain the simulation speed.

3) *Theoretical Distribution of Collision Angles*: A collision takes place when the centers of two spheres are one diameter apart. As shown in Fig. 8(a), a pair of colliding spheres of diameter D must have their centers both in a virtual cylinder; this cylinder is concentric with one of the spheres, has a diameter of $2D$, and is parallel to the relative velocities of the colliding spheres. The statistical distribution of the collision angles is described by a probability density $P(\theta, \phi)$, which means that the probability for the collision angles to fall within an infinitesimal range $(\theta \pm 0.5d\theta, \phi \pm 0.5d\phi)$ is $P(\theta, \phi)d\theta d\phi$. $P(\theta, \phi)$ is normalized such that an integral of $P(\theta, \phi)$ over the possible values for (θ, ϕ) equals one, i.e.,

$$\int_0^{\pi/2} \int_0^{2\pi} d\theta d\phi P(\theta, \phi) = 1. \quad (16)$$

To calculate $P(\theta, \phi)$, we used the fact that, relative to Sphere 1, the possible centers of Sphere 2 is uniformly distributed over the cross section of the cylinder. This gives

$$P(r, \phi) dr d\phi = \frac{r dr d\phi}{\pi D^2}. \quad (17)$$

The notation dr and $d\phi$ at both sides of the equation reminds us that the function P is a probability density. Because ϕ is uniformly distributed across $[0, 2\pi]$, we obtain

$$P(\phi) d\phi = \frac{1}{2\pi} \cdot d\phi. \quad (18)$$

By integrating $P(r, \phi)$ across $\phi = 0$ to 2π , we obtain

$$P(r) dr = \frac{2r dr}{D^2}. \quad (19)$$

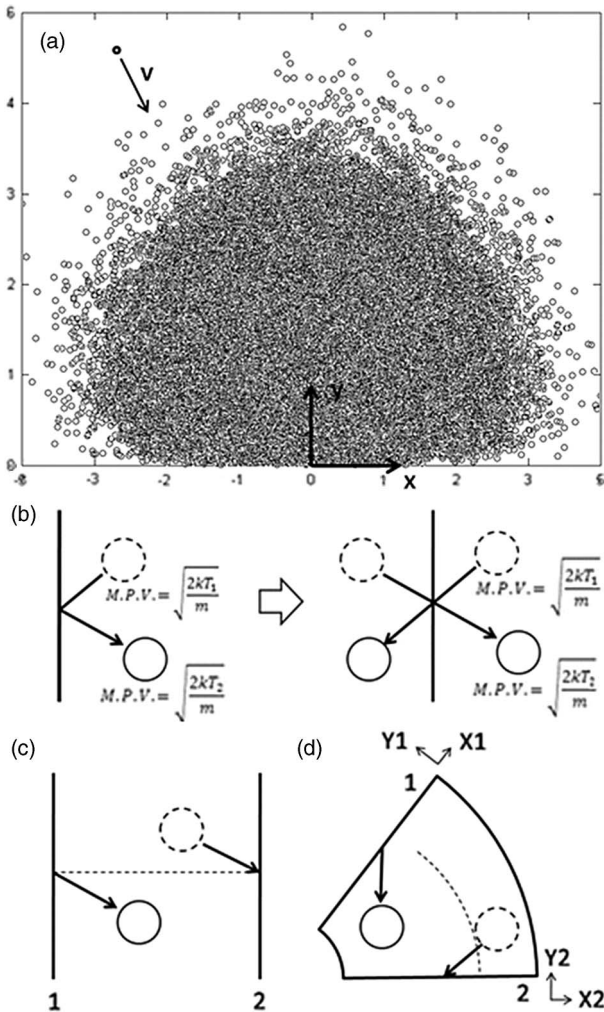


Fig. 9. (a) Simulation result showing the possible reflections of a particle by a thermal wall. (b) Illustration showing the equivalence between a DSMC thermal wall and an isothermal gas reservoir. (c) Linear periodic boundaries (1,2). (d) Angular periodic boundaries (1,2).

The probability densities $P(r)$ and $P(\theta)$ are related by $P(r)dr = P(\theta)d\theta$. Because $r = D \sin(\theta)$ and $dr = D \cos(\theta)d\theta$, the probability distribution for the collision angle θ becomes

$$P(\theta)d\theta = \sin(2\theta)d\theta. \quad (20)$$

Once the probability density of (θ, θ) is known, the post-collision velocities can be generated using a random generator (given by most simulation programs, such as MATLAB) that simulates the theoretical distribution. Fig. 8(b) shows the distribution of relative postcollision velocities of a pair of colliding spheres. The distributions of postcollision velocities are slightly biased toward the opposite sides of the incident direction of each particle.

4) *Interaction Between Particles and Simulation Boundaries:* Our DSMC model includes two types of boundaries: thermal walls and periodic boundaries (Fig. 9).

Thermal-wall boundary: A thermal wall is an isothermal boundary, at which the velocities of simulated molecules are reset based on the theoretical distribution of molecule speed at certain temperature. Upon the arrival of a particle, the thermal

wall randomly assigns a new velocity to the particle according to the biased Maxwell–Boltzmann distribution [22]

$$duP(u) = du \sqrt{\frac{m}{2\pi kT}} e^{-\frac{mu^2}{2kT}} \quad (21)$$

$$dvP(v) = dv \frac{m}{kT} v e^{-\frac{mv^2}{2kT}} \quad (22)$$

$$dwP(w) = dw \sqrt{\frac{m}{2\pi kT}} e^{-\frac{mw^2}{2kT}}. \quad (23)$$

The particle velocity (u, v, w) is relative to the surface, v is parallel to the surface normal, k is the Boltzmann constant, T is the temperature of the thermal-wall boundary, and m is the real mass of the gas molecule. Fig. 9(a) shows the possible movement of a particle reflected from a thermal wall. The wall is placed at $y = 0$. The particle came from $y > 0$ at a speed of arbitrary unit. The new velocity for the particle is biased, and $v_y > 0$. On the other hand, v_x and v_z follows Gaussian's normal distribution across $x = \pm\infty$.

A thermal wall is equivalent to a reservoir of particles at certain temperature. As shown in Fig. 9(b), a particle hitting the thermal wall can be considered leaving the boundary, and its reflection can be considered a new particle entering the simulation space.

Periodic boundary: Spatial periodicity can be used to reduce computation efforts. In simulating our four-bladed light mill, for example, we took into account the angular periodicity of the light mill and simulate only one quarter of the light mill's cross-sectional space; the simulation for the remaining three quarters are bypassed using two angular periodic boundaries. Each periodic boundary is paired with one counterpart boundary, which defines the opposite side of the simulation space. Each of the periodic boundaries has a unique coordinate system based on its surface normal vector. As shown in Fig. 9(c) and (d), a particle hitting a periodic boundary is shifted to the counterpart boundary, and its new position and velocity relative to the counterpart boundary are the same as their original values relative to the previous boundary.

B. Layout of Simulation Space

Fig. 10 shows the layout of the simulation space for our modeling. The simulation space covers only a quarter of the light-mill cross section; the angular periodicity of the light mill is taken into account by using two angular periodic boundaries. The simulation space is bounded by an isothermal reservoir at room temperature (25 °C), which forms an arc of radius D . We let D to be equal to four times the radius of the light mill. The hot and cold surfaces of the blade were setup as thermal-wall boundaries of constant temperatures T_{hot} and T_{cold} , respectively.

C. Simulation Results

Our DSMC model was implemented using MATLAB program. The effective hard-sphere constants, such as the effective radius of air, were given by [4]. Other programming details, such as the calculation of gas flow and the temperature gradient

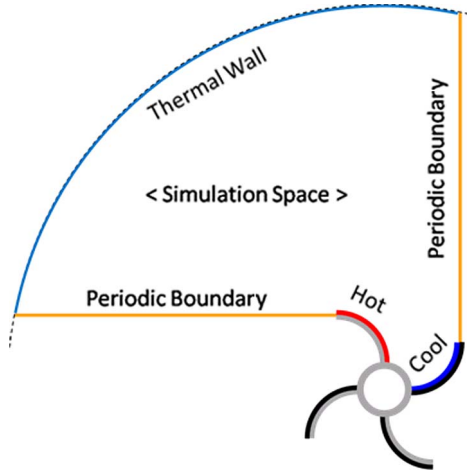


Fig. 10. Layout of the DSMC model.

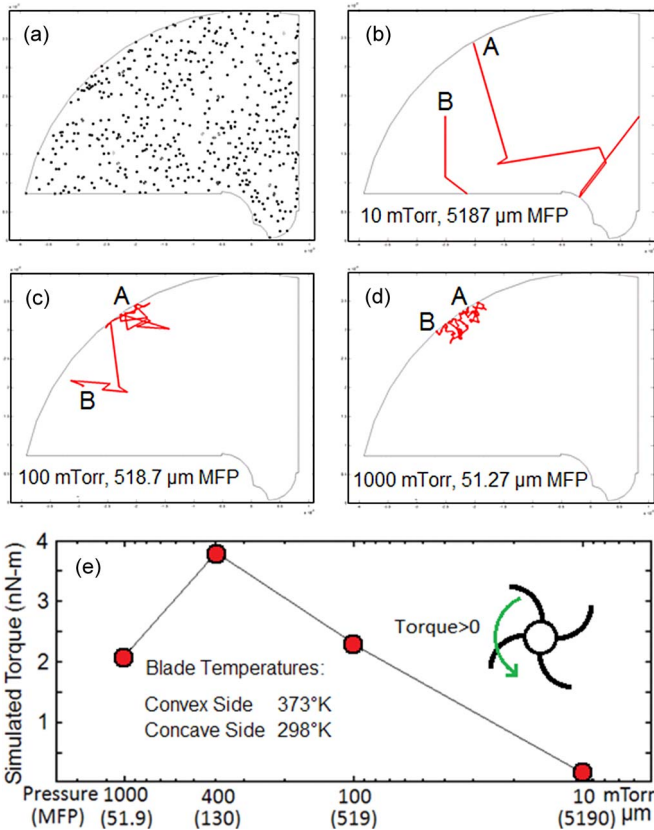


Fig. 11. Different DSMC results. (a) Movements of simulated gas molecules. (b)–(d) Collisions encountered by a gas molecule (from point A to B during a fixed time) at 10 100 and 1000 mtorr. (e) Heat-induced torque exerted to the light mill at different gas pressures.

and the selection of random pairs of gas molecules to undergo collisions, are based on the general principles of the DSMC method [21], [22]. Fig. 11 shows the different results from our simulation. Fig. 11(a) shows 500 simulated particles out of a total number of 500 000; through animation, we monitored the movement of particles, the collisions among particles, the passing of periodic boundaries, and the reflection of particles by thermal walls. Fig. 11(b)–(d) shows the simulated motions of single particles under different air pressures; each bending at

the particle route indicates one collision. The simulation results matched well with the theoretical values of MFP under different pressures.

We simulated the gas-applied torque to the light mill under several different pressures: 10, 100, 400, and 1000 mtorr. The torque at the light mill was calculated based on the striking of particles against the surfaces of the light mill

$$Torque(t) = 4 \cdot \frac{m_{air} N_{eff}}{\tau} \cdot \frac{\ell}{d} \sum_i^n \vec{x}_i \times \Delta \vec{v}_i \quad (24)$$

where n is the number of particles that strike the light mill during a simulation time step τ , t is the simulated time, m_{air} is the effective molecular weight of air, N_{eff} is the number of real molecules that each simulated particle represents, \vec{x}_i is the position where a particle strikes the light mill, ℓ is the axial length of the light mill (3 mm), d is the thickness of the simulated space, and $\Delta \vec{v}_i$ is the velocity change of the particle upon striking. The constant “4” takes into account the angular periodicity of the simulation space. The calculated values of the torque were averaged over the whole simulation time. We selected the simulated time for each modeling to be 1 ms, a time length at which the average value of the simulated torque became stable, and the calculated physical properties, such as temperature, formed smooth distributions over the simulation space.

To calculate the torque exclusively generated by the surface heating, we did a secondary simulation to calculate the gas dynamics of an unheated light mill: both sides of the blades were at room temperature (25 °C). The values of the torques calculated from the secondary simulation (which did not equal to zero due to inherited error of simulation) was subtracted from the result of the first group to give the heat-induced torque

$$Torque_{heat-induced} = Torque_{heated} - Torque_{unheated} \quad (25)$$

The simulated values of the heat-induced torque at the light mill [Fig. 11(e)] are counterclockwise (> 0), which would cause the light mill to rotate with the convex (hot) side retreating from the source of light. Comparing the calculated torques under the four different gas pressures, we found that the rotating speed is maximized when the pressure is near 400 mtorr, at which the MFP of air molecules is 130 μm. The simulated torque direction and the calculated optimized air pressure are both consistent with our experimental results.

D. Explanation of the Experimental Data Using Simulation Results

Fig. 12 shows the distribution of gas properties around the light mill at different pressures: 1000, 400, 100, and 10 mtorr. The color maps show the distribution of collision rates among gas molecules (as the number of collisions per second per sampling cell; red: high, blue: low). The streamlines indicate the flow of gas momentum (in kilogram-meter per second) induced by heating at the blades. For each blade, the temperature difference induces a gas flow from the concave (cooler) side to the convex (hotter) side. Following Newton’s third law,

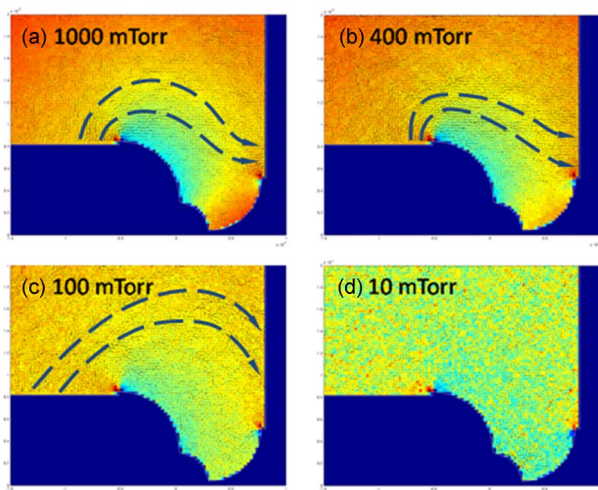


Fig. 12. Simulated heat-induced gas momentum at (a) 1000 mtorr, (b) 400 mtorr, (c) 100 mtorr, and (d) 10 mtorr; the streamlines are highlighted by the thick arrows. The heat-induced momentum streams fade at a low pressure, such as at 10 mtorr. The color maps indicate molecule collision rate (red: high; blue: low).

this result explains that the observed light-driven rotation of the light mill is caused by the recoil momentum from the heat-induced flow. We suggest the following mechanism to be behind the heat-induced convection of the surrounding gas.

- 1) The gas molecules heated by the convex (hotter) side of one blade tend to flow toward the concave (cooler) side of its neighboring blade due to a higher momentum.
- 2) Pushed by the hotter molecules from the convex surface of neighboring blade, the gas molecules on the concave (cooler) surface tend to flow toward the blade's edge.
- 3) The cooler gas molecules arriving at the edge tend to move toward the convex (hotter) side of the blade to fill the vacancy left by the gas molecules leaving the convex side.
- 4) The gas movement forms a cycle and generates a torque.

The effect of gas pressure (or gas density) on the light-mill rotation is also explained using the simulation results. We found that the strength and continuity of the heat-induced momentum flow strongly depends on the rate of collision (or the MFP of gas). At 1000 mtorr [Fig. 12(a)], for example, the heat-induced momentum flow is most continuous in the region next to the blade. The momentum field becomes weak and randomized in the region where the collision rate exceeds $1.4 \times 10^{17}/(\text{s} \cdot \text{m}^3)$ or where the particle density is above $3.4 \times 10^{22}/\text{m}^3$. At about $500 \mu\text{m}$ away from the blades, the elevated rate of particle collisions stops the spread of momentum flow; the higher rate of particle collisions in this region hinders the transfer of gas momentum.

At higher gas pressure (or lower MFP), the geometry of the light mill starts to affect the continuity of momentum flow. We found that when the MFP of gas molecules becomes smaller than the thickness of the light-mill blades, transport of gas momentum is hindered at the blade edge, and the flow becomes discontinuous; at such pressure, the collision rate is too high, and the gas molecules have insufficient mobility to maneuver

around the edge of the blade. This result is consistent with the conclusion given by [8].

Compared with the gas molecules at 1000 mtorr, the gas molecules at 400 mtorr [Fig. 12(b)] were able to expand the momentum flow to a wider range, further apart from the light mill and closer to the blade surface. The reduced pressure increases MFP, leads to higher mobility of gas molecules, and promotes efficient momentum transport. Further reduction of the gas pressure, however, generates negative effects to the development of heat-induced momentum flow [Fig. 12(c) and (d)]; the momentum flow fades when the pressure is too low. In the case of 10 mtorr [Fig. 12(d)], the heat-induced momentum becomes discontinuous over the simulation space. Under such a low pressure, the collision rate is too low, the molecules tend to move randomly, and the transport of gas momentum becomes inefficient. The fewer gas molecules per volume at low pressure also deliver less force to the light mill, leading to a smaller torque.

The aforementioned results explain the existence of an optimized gas pressure (or MFP) for the light-driven rotation. To maximize the strength of the heat-induced gas momentum and therefore maximize the torque at the blades, one should seek a balance between the rate of particle collisions and the mobility of the gas molecules: the rate of particle collisions (or gas pressure) should be high enough to efficiently transport gas momentum but low enough to yield sufficient mobility for the gas molecules.

V. CONCLUSION

We have created a light-powered micromotor by reinventing the light mill. This light mill has four curved blades, which are uniformly coated with dense nanoparticles for enhanced light absorption. Upon irradiation, this axially asymmetric shape leads to asymmetric photon heating, creates a temperature gradient across the blade, and leads to a heat-induced circulation of the gas molecules that causes the light mill to rotate. We applied this light-powered micromotor to rotate a small mirror, which directs a helium–neon laser beam to perform lateral scanning. We used DSMC method to investigate the working principle behind the observed light-induced rotation, in which the MFP of the gas molecules takes an important role, and the simulation results are consistent with our experimental data. The simplicity of the design and fabrication of this light mill promotes the development of light-powered motors of smaller dimensions, such as in the nanometer-size range.

ACKNOWLEDGMENT

S. Chen would like to thank Texas Instruments for the donation of the DMD tool kit and Intel's High Education Program for the computer support.

REFERENCES

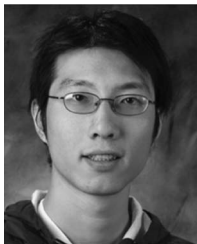
- [1] Y. Yu, M. Nakano, and T. Ikeda, "Photomechanics: Directed bending of a polymer film by light," *Nature*, vol. 425, no. 6954, p. 145, Sep. 2003.
- [2] T. Muraoka, K. Kinbara, and T. Aida, "Mechanical twisting of a guest by a photoresponsive host," *Nature*, vol. 440, no. 7083, pp. 512–515, Mar. 2006.
- [3] M. J. Madou, *Fundamentals of Microfabrication: The Science of Miniaturization*, 2nd ed. New York: CRC Press, 2001.

- [4] M. Ferrari, R. Bashir, and S. Wereley, *BioMEMS and Biomedical Nanotechnology*. New York: Springer-Verlag, 2006.
- [5] R. Osiander, M. A. G. Darrin, and J. Champion, *MEMS and Microstructures in Aerospace Applications*. Boca Raton, FL: CRC Press, 2006.
- [6] M. D. Feldman, T. E. Milner, S. C. Chen, J. H. Kim, L. H. Han, J.-H. Oh, and H. Lee, "Catheter imaging probe and method," U.S. Patent 7711 413, May 4, 2010.
- [7] A. F. Fercher, W. Drexler, C. K. Hitzenberger, and T. Lasser, "Optical coherence tomography—Principles and applications," *Rep. Prog. Phys.*, vol. 66, no. 2, pp. 239–303, Jan. 2003.
- [8] A. Einstein, "Zur theorie der radiomerkraft," *Z. Phys.*, vol. 27, no. 1, pp. 1–6, 1924.
- [9] J. C. Maxwell, "On stresses in rarefied gases arising from inequalities of temperature," *Proc. R. Soc. Lond.*, vol. 27, pp. 304–308, Mar. 1878.
- [10] L. H. Han, S. M. Wu, J. C. Condit, N. J. Nate, M. D. Feldman, T. Milner, and S. C. Chen, "Light-powered micromotor driven by geometry-assisted, asymmetric photon-heating and subsequent gas convection," *Appl. Phys. Lett.*, vol. 96, no. 21, p. 213 509 (1-3), May 2010.
- [11] L. H. Han, G. Mapili, S. C. Chen, and K. Roy, "Projection micro-printing of three-dimensional scaffolds for tissue engineering," *J. Manuf. Sci. Eng.*, vol. 130, no. 2, p. 021 005 (1-4), Apr. 2008.
- [12] S. M. Wu, L. H. Han, and S. C. Chen, "Three-dimensional selective growth of nanoparticles on a polymer microstructure," *Nanotechnology*, vol. 20, no. 28, p. 285 312 (1-4), Jun. 2009.
- [13] D. J. Hellebusch, K. W. Wu, E. K. Kim, K. Lu, L. Tao, K. M. Liechti, J. G. Ekerdt, P. S. Ho, W. Hu, and C. G. Willson, "Interfacial adhesion studies for step and flash imprint lithography," *Proc. SPIE*, vol. 6921, p. 692 10E (1-12), Mar. 2008.
- [14] L. H. Han, W. Wang, Y. L. Lu, R. J. Knize, K. Reinhardt, J. R. Howell, and S. C. Chen, "Analytical and experimental investigation of electromagnetic field enhancement among nanospheres with Varying Spacing," *J. Heat Transf.*, vol. 131, no. 3, p. 033 110 (1-6), Mar. 2009.
- [15] S. Calvert and H. M. Englund, *Handbook of Air Pollution*. New York: Wiley, 1984, p. 103.
- [16] D. Vokrouhlický, D. Nesvorný, and W. F. Bottke, "The vector alignments of asteroid spins by thermal torques," *Nature*, vol. 425, no. 6954, pp. 147–151, Sep. 2003.
- [17] See video at supplementary material (online) for the rotation of light mill and scanning mirror.
- [18] A. Alexandrou, *Principles of Fluid Mechanics*, 2nd ed. Upper Saddle River, NJ: Prentice-Hall, 2001, pp. 203–208.
- [19] K. Huang, *Statistical Mechanics*, 2nd ed. New York: Wiley, 1987, p. 125.
- [20] K. Huang, *Statistical Mechanics*, 2nd ed. New York: Wiley, 1987, p. 93.
- [21] G. A. Bird, *Molecular Gas Dynamics*. Oxford, U.K.: Clarendon, 1976, pp. 17–21.
- [22] A. L. Garcia, *Numerical Methods for Physics*, 2nd ed. Upper Saddle River: Prentice-Hall, 1994, pp. 319–347.



Li-Hsin Han received the B.S. and M.S. degrees in mechanical engineering from National Taiwan University, Taipei, Taiwan, in 1996 and 1998, respectively, and the Ph.D. degree in mechanical engineering from The University of Texas at Austin, in 2009.

He is currently a Postdoctoral Fellow in the Department of Orthopaedic Surgery, Stanford University, Stanford, CA. His research covers mechanical-system design, polymeric microdevices, nanoscaled photonics, biomaterials, and biomimetic microstructures for tissue engineering.



Shaomin Wu received the B.S. degree in materials science from Fudan University, Shanghai, China, in 2001, the M.S. degree in electrical and computer engineering from the University of California, Santa Barbara, in 2004, and the Ph.D. degree in materials science and engineering from The University of Texas at Austin, in 2010.

His research interests include optoelectronic devices, nanofabrications, and plasmonic solar cells. He has two years of industry experience in compound-semiconductor growth.



J. Christopher Condit received the B.S. degree in electrical engineering from The University of TX at Austin, where he is currently working toward the M.S. degree in biomedical engineering.

He is currently serving as CEO of SpectraPhase, Austin, TX, an early-stage medical device company focusing on fiber-optical catheter monitoring. His interest is working to bring novel biomedical-technology applications to market as medical devices.



Nate J. Kemp received the B.S. degree in electrical engineering from the University of Colorado, Colorado Springs, and the M.S. and Ph.D. degrees in biomedical engineering from The University of Texas at Austin.

Since 2006, he has been a Research and Development Engineer and Chief Architect for OCT (optical coherence tomography) systems with CardioSpectra and Volcano Corporation, Billerica, MA.



Thomas E. Milner is a Professor in the Department of Biomedical Engineering, The University of Texas at Austin, and cofounder of CardioSpectra acquired by Volcano Corporation, Billerica, MA. His research is directed toward the development of novel optical tomographic imaging modalities and laser surgical procedures for diagnosis and treatment of disease in humans. In collaboration with dermatologists and industrial affiliates, his group is investigating application of these technologies in the clinic.



Marc D. Feldman received the B.S. degree from Duke University, Durham, NC, in 1977, and the M.D. degree from the University of Pennsylvania School of Medicine, Philadelphia, in 1981.

He completed his Internship and Residency at Billings Hospital, University of Chicago, Chicago, IL. He was a Clinical and a Research Fellow in cardiology at Beth Israel Hospital, Harvard Medical School, Boston, MA. He is currently a Professor of medicine and engineering and the Director of the Cardiac Catheterization Laboratories, Division of

Cardiology, The University of Texas Health Sciences Center, San Antonio. He is also an Adjunct Professor at The University of Texas at Austin.



Shaochen Chen received the B.S. degree from Tsinghua University, Beijing, China, in 1989 and the Ph.D. degree from the University of California at Berkeley in 1999.

He was a Professor and the Pearl D. Henderson Centennial Endowed Faculty Fellow in Engineering in the Mechanical Engineering Department, The University of Texas at Austin. He is currently a Professor in the Nanoengineering Department, University of California, San Diego (UCSD). He is also a Faculty Member of the Institute of Engineering in

Medicine at UCSD. From 2008 to 2010, he served as the Program Director of the Nanomanufacturing Program of the National Science Foundation (NSF), where he directed the frontiers of nanomanufacturing research at NSF and managed 150 active grants of the program. His primary research interests include biomaterials and biofabrication, nanoregenerative medicine, laser nanomanufacturing, nanophotonics, plasmonics and metamaterials, and bio- and nanomechanics.